Mechanical Behavior Characterization of a Stainless Steel Dissimilar Metal Weld Interface : In-situ Micro-Tensile Testing on Carburized Martensite and Austenite

G. Ben Salem, E. Héripré, P. Bompard, S. Chapuliot, A. Blouin, C. Jacquemoud

Mechanical behavior characterization of a stainless steel dissimilar metal weld interface : In-situ micro-tensile testing on carburized martensite and austenite

G. Ben Salem[a,b,c,*], E. Héripré[b], P. Bompard[b], S. Chapuliot[a], A. Blouin[a], C. Jacquemoud[c]

[a] *FRAMATOME, 1 Pl. Jean Millier, 92400 Courbevoie, France*
[b] *Laboratoire MSSMat, UMR CNRS 8579, CentraleSupelec, 3 Rue Joliot Curie, 91190 Gif-sur-Yvette, France*
[c] *DEN-Service d´études mécaniques et thermiques (SEMT), CEA, Université Paris-Saclay, F-91191 Gif-sur-Yvette, France*

Abstract

Stainless Steel Dissimilar Metal Welds (SS DMW) between low-alloy steel 18MND5 and austenitic 316L stainless steel are critical junctions in the currently operating reactors because of their heterogeneous microstructure and mechanical properties. The presence of a narrow hard layer of carburized martensite and austenite in the ferritic-austenitic interface creates an important hardness gradient which affects the crack behavior of the SS DMW.

In order to evaluate the plastic properties of this hard layer, a micro tensile testing method was developed. Tensile specimens of 15 x 80 x 6 μm were extracted from the martensitic and carburized austenitic layers by focused ion beam (FIB) micro-processing and tested using an in-situ tensile testing device. The tensile grips were machined in a tungsten rotating needle and a Molybdenum lift-out grid. The displacements and rotation of the components were enabled by a rotating motor and three piezoelectric displacement plates. The load was measured with a load cell and a platinum FIB deposition was used to measure local strain in the specimen during the test through digital image correlation (DIC).

Isotropic elasto-plastic constitutive laws for the martensite and carburized austenite were obtained from the true strain-stress curves calculated from the micro-tensile tests. It was found that the corresponding plastic properties were in a good agreement with nanoindentation measurements and with values obtained from macroscopic tensile tests on crossweld specimens machined perpendicularly to the ferritic-austenitic interface using laser beam local section measurements.

Keywords: Dissimilar Metal welds; Martensite; Carburized austenite; plastic properties; Micro-tensile testing;

*Corresponding author. Tel.: +33-610-68-1105

1. Introduction

Stainless Steel Dissimilar Metal Welds (SS DMW) between low-alloy steel 18MND5(~A533) and austenitic 316L stainless steel are widely used within the French nuclear power plants, where they connect the main components to the primary circuit pipes (Fig. 1-a). Because of their highly heterogeneous microstructure, mechanical properties [1, 2, 3] and the existence of residual stresses [4], these components are critical for the integrity of the currently operating reactors [5, 6, 7].

The microstructure of these DMW was explored by F.Mas [1] and characterized around the Ferritic-Austenitic interface. The welding process and the post-weld heat-treatment generate a hard thin layer (between 50 μm and 200 μm width) of carburized martensite and austenite in the vicinity of the fusion line (FL). The resulting high mechanical properties gradients greatly affect the stress and strain distribution around the FL and the damage mechanism in a fracture test [1, 2, 6, 7]. It is therefore important to precisely measure the plastic properties variation (yield stress and hardening exponent) around the FL in order to correctly model the overall transverse behavior of the DMW.

Plastic behavior characterization of the hard layer where tensile specimens can not be extracted is a real challenge in SS DMW. In addition to their limited width, the important local hardness in comparison to the surrounding soft layers (ferritic decarburized HAZ and austenitic buttering) prevents any plastic deformation in a macroscopic tensile specimen machined perpendicularly to the FL [1]. On the other hand, nanoindentation which is a local method to probe mechanical properties at a submicron scale seems to be suitable for this case but presents many limitations : plastic properties are identified by reverse algorithm based on functions originating from FE simulations which are performed with some assumptions (perfectly shaped indents...). Furthermore, this method gives highly dispersed results for materials with heterogeneities whose size is comparable to the indent size or with coarse microstructure [1].

The present study aims to present a new characterization method with in-situ tensile testing to measure the plastic properties of the martensitic and carburized austenitic layers. The samples extracted from the different layers were fabricated with FIB micro-processing and tested using a homemade in-situ micro-mechanical tensile testing machine. The measured values for the yield stress and hardening exponent are compared to the elasto-plastic constitutive laws identified by nanoindentation [1, 2] and by macroscopic tensile testing on tensile

E-mail address: ghassen.ben-salem@ecp.fr

specimens machined perpendicularly to the FL using laser beam section measurement along the specimen.

2. Micrographic study of the DMW

The DMW under consideration is a 18MND5/316L weld with a 309L/308L buttering. The buttering is made on the ferritic component surface and is composed of several layers (i.e., the first layer is made of 309L weld metal, the rest are made of 308L weld metal), then, the buttering is welded to a 316L stainless steel "safe-end" with a filling of the V groove by austenitic weld metal. Finally, the "safe-ends" are connected to the 316L stainless steel piping by onsite homogeneous welding (Fig. 1-b).

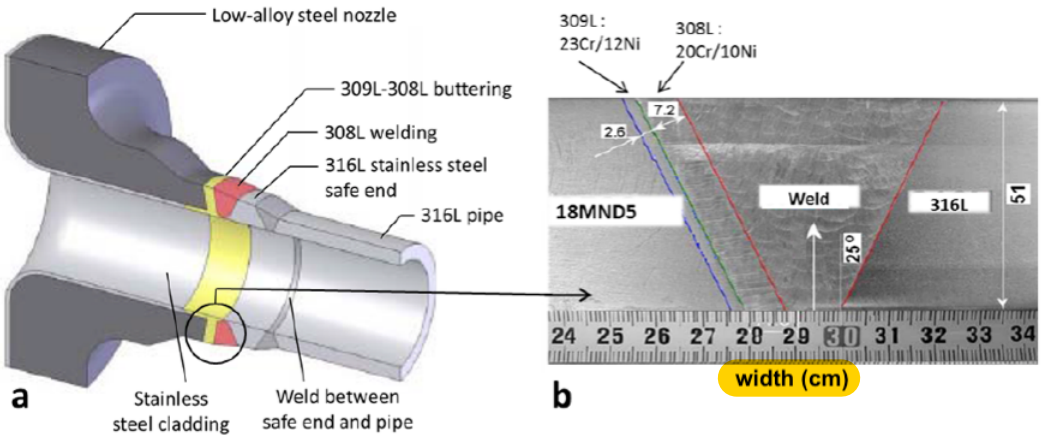

Figure 1: (a) Schematic of a connection between a low-alloy steel component and a stainless steel pipe; (b) Geometry and constituents of a dissimilar steel weld [1]

This paper focuses on the 18MND5/309L interface of the DMW. Its microstructure, studied in [1], is presented in the as-welded state (after the welding process) and after a post-weld heat treatment of 8h at 610°C (PWHT).

Based on WDS (Wavelength X-ray Spectrometry) profiles measured across the interface in the as-welded state, Mas [1, 3] has characterized the different microstructures formed during the welding process (Fig. 2-a):

- On the ferritic base metal (BM) side (18MND5), a Heat Affected Zone (HAZ) characterized by its bainitic microstructure is formed.
- A thin transition layer, along the fusion line, which is composed of a thin martensitic layer and a fully austenitic zone of about 100 μm wide.
- On the weld metal side (309L), the austenitic buttering is characterized by its two-phase δ-γ microstructure and the presence of dendrites.

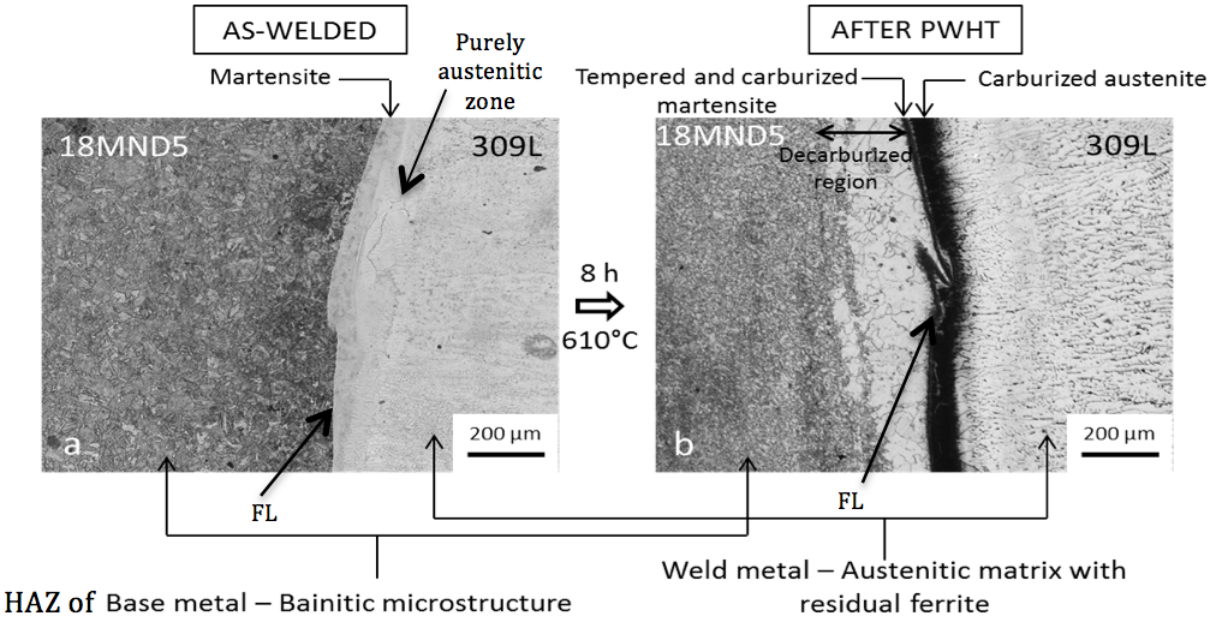

Figure 2: Optical micrograph of the dissimilar interface : (a) in the as-welded state (b) after PWHT [1]

The martensitic layer formed at the interface results from a combination of the rapid cooling subsequent to welding and the local enrichment of the base metal in Cr and Ni during the welding process [8], [9], [10], [12]. Energy Dispersive X-ray Spectrometry (EDS) measurements across the ferritic-austenitic interface (Fig. 3-b) reveal the presence of an intermediate zone, whose chemical composition corresponds to a mixture between mainly the ferritic steel and the austenitic buttering. This intermediate zone corresponds to the martensitic band since it is situated between the ferritic HAZ, whose chemical composition is the same as the ferritic base metal, and the fully austenitic zone, which is characterized by the absence of dendrites (Fig. 3-b). High hardness was also measured in this transition layer [11], [13]. The fully austenitic zone shows a microstructure typical of a primary austenite solidification grown on the ferritic base metal former heat treated austenitic grains, whereas the deposit material with a two-phase dendritic microstructure is typical of a primary ferrite solidification.

After the welding process, the DMW undergoes a heat-treatment at 610°C for 8 hours in order to relax the welding residual stresses and temper the bainitic HAZ and martensitic layer. Mas[1, 3] shows that carbon diffusion from the ferritic low-alloy steel side (18MND5) to the austenitic high-alloy side (309L) is triggered at this temperature resulting in important microstructural heterogeneities over short distances around the interface. The martensitic layer and the fully austenitic zone undergo a carbon enrichment together with nucleation and growth of carbides whereas decarburization of the 18MND5 base metal results in the formation of a narrow decarburized ferritic band (Fig. 2-b). The hardened region (hard layer) composed of the carburized martensite

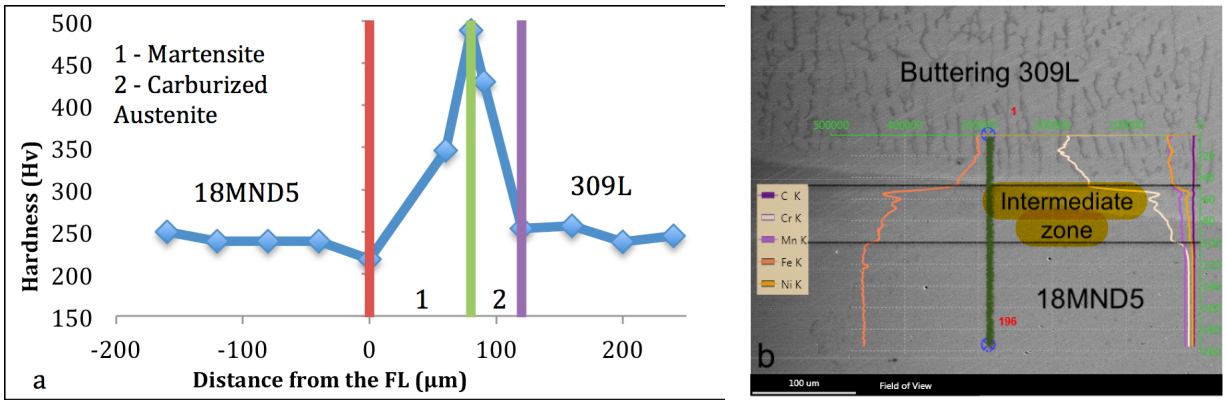

Figure 3: (a) Micro-hardness profile around the FL after PWHT (b) EDS profile on a line across the 18MND5/309L interface after PWHT

and the carburized austenite is located between two much softer layers (decarburized ferritic region on one side and the weld metal 309L on the other side) which creates a strong local hardness gradient (Fig. 3-a). Coupled with the presence of a large population of defects (carbides at the grain boundaries), the 18MND5/309L interface could be a potential weak zone in the SS DMW, thus it is necessary to characterize its mechanical behavior.

In the following sections, we focus on the mechanical behavior characterization of the martensitic and carburized fully austenitic layers at room temperature.

3. Mechanical characterization of the hard layer with nanoindentation and macroscopic tensile testing

3.1. Nanoindentation

Mas [1, 2] probed the plastic properties of thin layers (decarburized layer, Martensite, Carburized austenite), where tensile specimens could not be extracted, with nanoindentation. Two different indenters (Berkovich and cube corner) were used and the local plastic properties were identified by reverse algorithm based on Bucaille's method [14] with correction for friction. The method required each Berkovich indent to be associated with another cube corner indent to determine one set of plastic properties (yield strength σ_y, hardening exponent n). The results obtained are summarized in table 1.

Table 1: Mechanical properties from nanoindentation by Bucaille's method [1]

	E (GPa)	σ_y (MPa)	n
Martensite	244	1472-1797	0
Carburized austenite (15 μm from martensite)	235	2166-2509	0
Carburized austenite (40 μm from martensite)	235	964-1021	0.11-0.13

The results show a high scatter in the Martensite and carburized austenite which is due to the heterogeneous

microstructure and the presence of a large population of carbides. Moreover, an important drop of hardness occurs in the carburized austenite when moving towards the stainless steel away from the martensite/austenite interface. This layer had therefore to be divided into two subregions characterized by a strong gradient in mechanical properties : a mean σ_y value of 2300 MPa and n = 0 at 15 μm from the martensitic band and a much softer region at 40 μm with a mean σ_y = 1000 MPa and n = 0.12. The martensitic band is characterized by a mean yield strength of 1650 MPa and doesn't show much hardening (n = 0).

Although these values give a good indication of the local plastic behavior in the hard layer, some uncertainty factor has to be considered because of the limitations of nanoindentation measurement. In addition to the non-ideality of the indent tip and the different assumptions previously discussed, both the pairing of the indents, which relies on the assumption that the material under each indent is perfectly identical, and the heterogeneities of the microstructure increase the scatter of the data. The reliability of this method is nonetheless better in the martensitic band, where the grain size (<10 μm) is smaller than the indent tip size, compared to the carburized austenite. Because of the coarse microstructure in the austenitic side (grain size up to 100 μm), with nanoindentation, only one grain can be probed at the same time and the orientation effects cannot be neglected. The important hardening in the second subregion and the anisotropic behavior of the material also increase the difficulty of extracting plastic properties from nanoindentation tests since the induced stress state and plastic zone around the indent are 3 dimensional [15], [16]. In order to confirm the values obtained for the martensitic layer and carburized austenite (yield stress σ_y and hardening exponent n) with nanoindentation, an attempt has been made to extract the plastic properties of the hard layer with macroscopic tensile testing using laser local section measurements and numerical simulation.

3.2. Tensile testing of a smooth crossweld specimen

In order to characterize the welded junction, smooth specimens were machined in a representative SS DMW mock up through the weld (crossweld) (Fig. 4). A new measurement system, developed in the LISN laboratory of the CEA (French atomic commission) by Ancelet [17], was used to test the crossweld specimens. The use of two laser micrometers equipped on a tensile machine allows measuring the local diameter variation along the specimen during the tensile test.

The axial stress and strain are then calculated locally along the tensile axis using the following formulas for

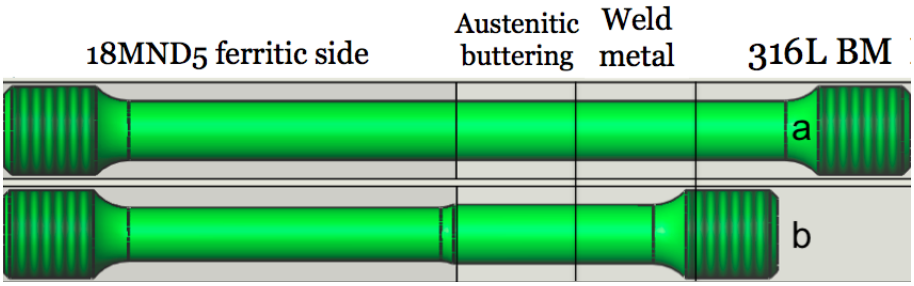

Figure 4: Machining of tensile specimens in a SS DMW mock-up : (a) crossweld specimen with homogeneous diameter and (b) crossweld specimen with variable diameter

an axisymmetric tensile specimen :

$$\epsilon = ln(\frac{S_0}{S}) = -2.ln(\frac{a}{a_0}) \tag{1}$$

$$\sigma_{true} = \frac{F}{S} \tag{2}$$

where ϵ and σ_{true} are the local strain and stress, a is the specimen local radius, a_0 the specimen initial radius, F is the load and S the local section.

Moreover, a Bridgman correction of the true stress is performed for the specimen position where necking occurs using the following formula :

$$\sigma_{true} = \frac{F}{S}.B(\frac{a}{R}) \tag{3}$$

where B is a Bridgman function to take into account the stress multiaxiality due to the local curvature R during the instability phase (necking) [17].

For the crossweld specimen, this measurement system was used to calculate a true strain-stress curve for each material and a constitutive behavior law was obtained for each macroscopic layer (ferritic base metal, ferritic HAZ, austenitic buttering, austenitic weld) assuming that the materials have an isotropic elasto-plastic behavior. In this context, the yield criterion is adopted as the criterion of von Mises.

It must be noted that only the axial stress (in the tensile direction) is considered in the previous stress formula. So in order to extract the plastic properties of the material from the experimental strain-stress curve,

we have to verify that shear stress remains negligible, which is the case for the macroscopic layers in the crossweld specimen, but not for thin hard layers subjected to transverse compression.

The austenitic buttering 308L/309L being softer than the ferritic steel, crossweld specimens with a homogeneous diameter (8 mm) (Fig. 4-a) are used to characterize the austenitic side of the weld. Specimens with variable diameters (smaller diameter of 7.2 mm in the ferritic side vs 8 mm in the austenitic side) (Fig. 4-b) allow the deformation of the ferritic base metal and HAZ and are therefore used to characterize the ferritic side of the weld. Moreover, the diameter variation was optimised with numerical simulation of the tensile tests (Fig. 6-a) using the constitutive behavior laws identified in [1].

Figure 5 shows an example of behavior constitutive laws identification with the crossweld specimen with variable diameter. The ferritic base metal, ferritic HAZ, austenitic buttering and weld metal were characterized using the profilometry measurement during the tensile test. The local diameter variation in the hard layer (martensitic band and carburized austenite) is negligible compared to the much softer layers near the interface (decarburized HAZ and austenitic buttering). This strain gradient creates important shear stress in the hard layer and a direct identification of a constitutive behavior law is therefore not possible in the same way than for the macroscopic layers.

In order to identify the plastic properties and a constitutive behavior law for the hard layer, a reverse method using numerical simulation was applied.

The tensile test of the specimen with variable diameter (Fig. 5-a) was modeled using a finite element analysis with Cast3m software [18]. The mesh used for the modeling and the associated boundary conditions are presented in figure 6-a. The modeling was performed with 2D axisymmetric calculation using quadratic elements QUA8 and assuming large strains and large displacements. The boundary conditions were as following:

- All the displacements are locked for line CD;
- The line EC is the axisymmetric axis;
- The loading displacement along the tensile axis is imposed on line EF.

The material behavior for each of the four macroscopic layers was given by the constitutive laws in figure 6-a and their width was determined based on the profilometries measurements during the tensile test (Fig. 5-a). For the hard layer, a perfectly plastic behavior law with no hardening was assumed for both the martensitic and carburized austenitic layers. The position of the martensitic/austenitic interface was measured on the specimen after chemical etching to reveal the FL and the width of the hard layer (120 μm) was measured with a hardness profile across the interface (Fig. 3-a).

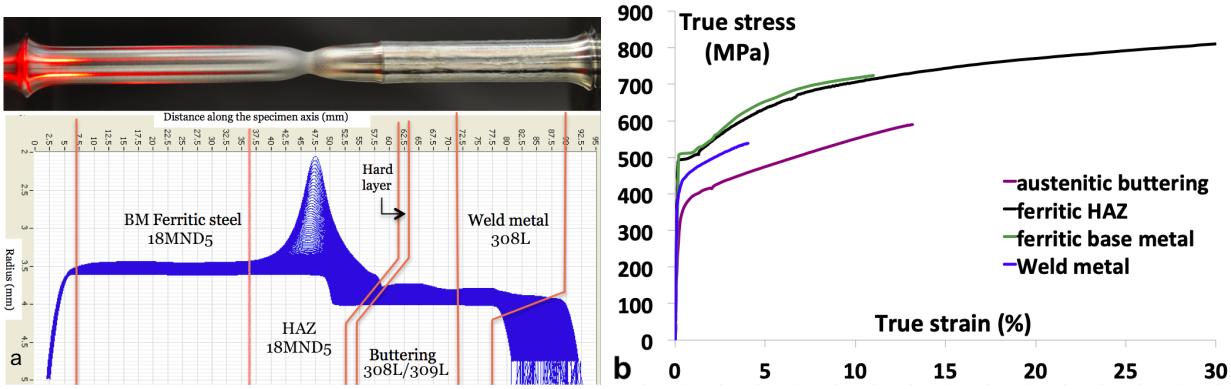

Figure 5: (a) Profilometries measurement during the tensile test on a crossweld specimen with variable diameter (b) Constitutive isotropic elasto-plastic laws calculated for the macroscopic layer of the SS DMW

The numerical model was validated by comparing the experimental and numerical engineering strain-stress curves as well as the diameter profilometries calculated numerically and measured with the two laser micrometers at two different moments in the tensile test : when the load reached its maximum value, and at failure (Fig. 6-b).

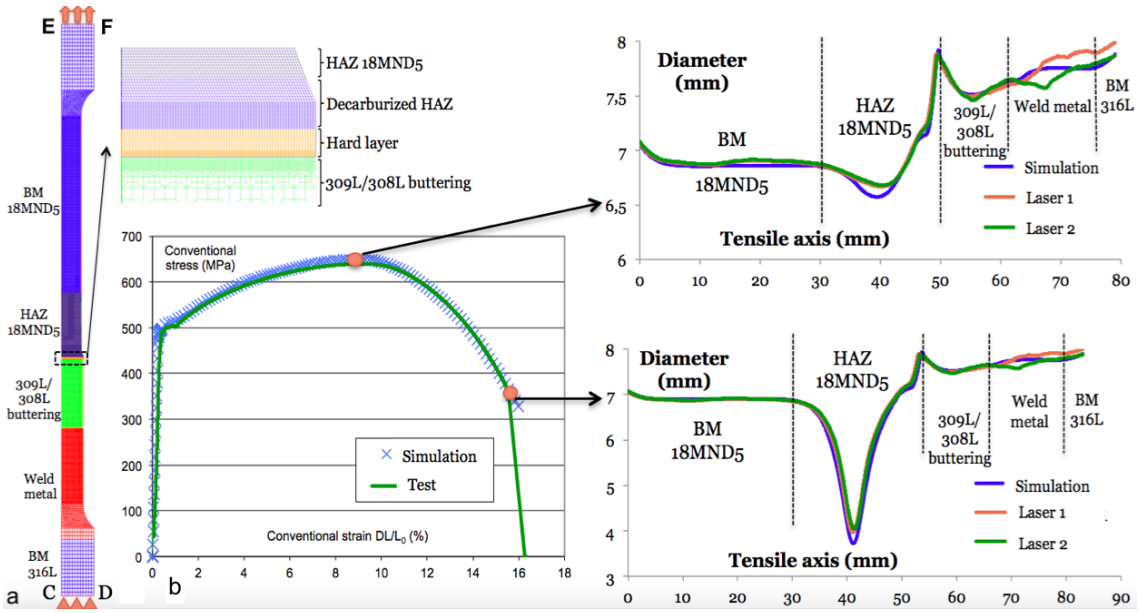

Figure 6: Numerical simulation of the crossweld specimen with variable diameter : (a) Numerical model mesh and boundary conditions (b) Comparison between experimental and numerical engineering stress-strain curves and diameter profiles

Then several simulations were performed with different yield stress values for the hard layer. For each simulation, local strain-stress curves were calculated using equations 1 & 2 at different positions in the hard layer : on the FL and at 75 μm from the FL in the martensitic layer. These curves were then compared to the

corresponding experimental curves.

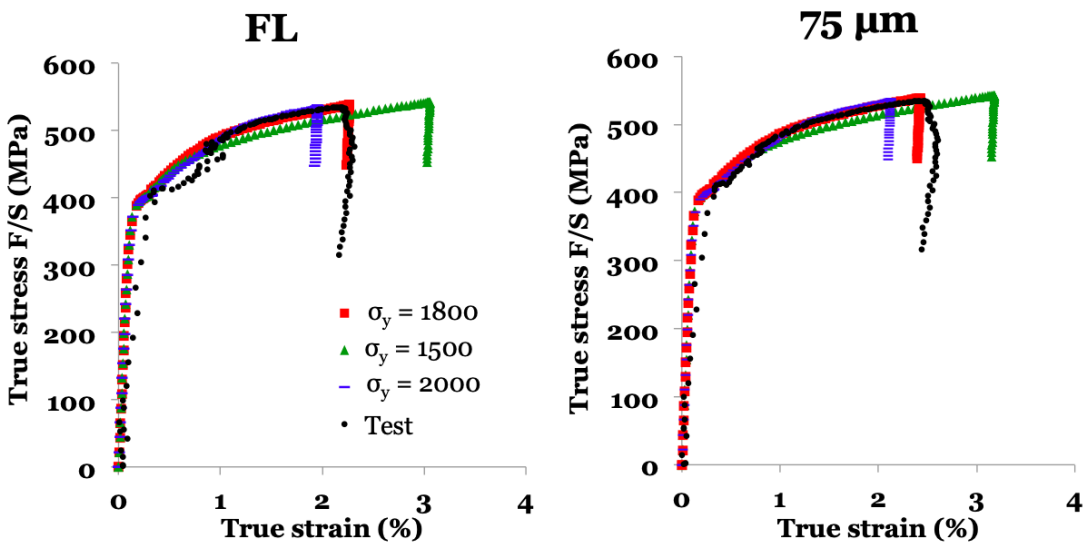

Figure 7: Comparison between experimental and numerical true stress-strain curves at different positions in the hard layer for different hard layer yield stresses a) on the FL and b) at 75 μm from the FL

Figure 7 shows that a good agreement was obtained for a yield stress of 1800 MPa for the two positions at the FL and at 75 μm in the hard layer. The numerical and experimental curves are also similar after the yielding point which validates the perfect plasticity assumption of the hard layer made for the numerical simulations.

The yield stress of 1800 MPa is an average value for both martensitic and carburized austenite layers constituting the hard layer. This value is also in good agreement with the values measured in section 3.1 by nanoindentation in the martensitic band (1650 MPa) and the first subregion of the carburized austenite (2300 MPa), which is a first validation of these results.

Based on the macroscopic tensile tests and the numerical calculations performed in this section, the hard layer can be characterized by a reverse identification method but only for a very limited strain range (<3%). This is due to the tensile specimen failure before any large strain could be measured in the hard layer which was a direct consequence of the presence of two much softer layers (decarburized HAZ and austenitic buttering) around the interface.

In order to characterize the martensitic and carburized austenitic layers for a larger strain range, tensile tests were performed on ”homogeneous” specimens machined in the hard layer at a submicron scale, which is the focus of the following section.

4. Mechanical characterization of the hard layer with in-situ tensile testing

Small-scale mechanical testing techniques have been extensively explored for engineering applications. Micro-tensile testing in particular has proven to be a valuable technique to characterize materials at small dimensions and measure the strain-stress curve up to failure. However, the use of this technique on thin regions has been quite challenging and several experimental hurdles had to be overcome to do proper tensile testing of materials in the meso-scale dimension regime (i.e. a range of a few μm to tens of μm). The manufacturing of sensitive equipment for the test (grips), the fabrication of the specimen or the choice of measurement methods for stress and strain calculation are among the technical difficulties which have to be taken into account to properly measure mechanical properties.

In the past, a few tensile tests have been performed especially on single crystal specimens, such as those conducted on single-crystal copper specimens by Kiener et al. [19] to explore the size-dependance of crystal plasticity, or on single-crystal Fe samples by Bhattacharyya et al. [20] to observe slip phenomena. The effect of irradiation on materials was also studied by in-situ micro tensile testing on irradiated and implanted single crystal nickel films by Reichardt et al. [21] or on irradiated stainless steel by Vo et al. [22]. Katsuhiko et al. [23] also performed in-situ tensile tests on bi-crystal Fe-Mn-P alloy specimens to evaluate the grain boundary strength after P segregation.

In this context, the testing of specimens from the martensitic band or the carburized austenite requires several precautions. Because of the limited width of these layers, the specimens had to be entirely machined and tested separately from the macroscopic weld sample, which required the machining of two grips on both sides of the specimen. The following requirements had to be taken into account in order to do a proper in-situ tensile testing on these materials :

- Small specimens with a tensile geometry (dogbone for example) must be fabricated separately from the original macroscopic sample;
- Special attention must be given to the specimen manipulation to avoid losing it during the test preparation;
- Two grips must be machined separately from the specimen;
- The specimen has to be fixed in the grips during the tensile test;
- Loads and displacements have to be measured during the test.

To answer these needs, a micro-testing machine was developed in the MSSMat Laboratory with the collaboration of Framatome. The specimens were fabricated using a FEI Helios Nanolab 660 FIB/SEM equipped

with an easylift micromanipulator and a gas induced system for Platinum deposition. They were then tested on the micro-tensile device.

4.1. Experimental setup

The testing machine used for the in-situ tensile tests is presented on figure 8.

The machine frame was 3D printed with plastic materials and specific parts were machined to fix the different components for the specimen and grips machining. The frame was also covered with an electrically conductive spray paint to avoid drift issues during electronic and ionic imaging or EDS and EBSD measurements.

A load cell with a capacity of 50 g (0,5 N) and calibrated using a dead weight calibration was used to measure loading during the test. A Molybdenum thin foil (a lift-out grid was used) (Fig. 8) was fixed on the load cell side of the tensile device and was used to machine one of the specimen grips (grip on the right side of figure 9-b). The fixing component containing the lift-out grid was attached to the extremity of the strain gauge load cell so that the load is transmitted from the specimen to the load cell via the lift-out grid during the tensile test. The other specimen grip (grip on the left side of figure 9-b) was machined in a tungsten needle mounted on a rotating motor (Fig. 8), which is also necessary for the specimen fabrication.

Finally, the displacement in each direction was obtained with piezoelectric displacement plates (Fig. 8) characterized by a displacement resolution of 1 nm and a speed resolution of 1 μm/s. The loading direction (X direction) was also controlled with an encoder to precisely measure the specimen displacement during the test. More details on the in-situ tensile machine components and the sample preparation are given in [24].

4.2. Sample preparation

In order to distinguish the martensitic layer and fully austenitic zone in the interface, a weld sample was prepared by classical polishing techniques, the last step consisting of prolonged polishing in a colloidal silica suspension which reveals the martensitic laths and the ferritic grains in the ferritic HAZ (Fig. 10). The polishing also clearly reveals the ferritic dendrites in the austenitic side making it possible to distinguish the fully austenitic zone from the two-phase δ-γ microstructure of the buttering.

The first step for the specimen machining was the extraction of a block (30 x 100 x 15 μm) from the sample with FIB milling. The extracted block was welded to a micromanipulator needle before the last cut was performed. The block was then transported and welded to the rotating needle tip with FIB induced deposition of Pt. The tensile specimen was finally machined by rotating the needle mounted on the rotating motor (Fig. 9-a).

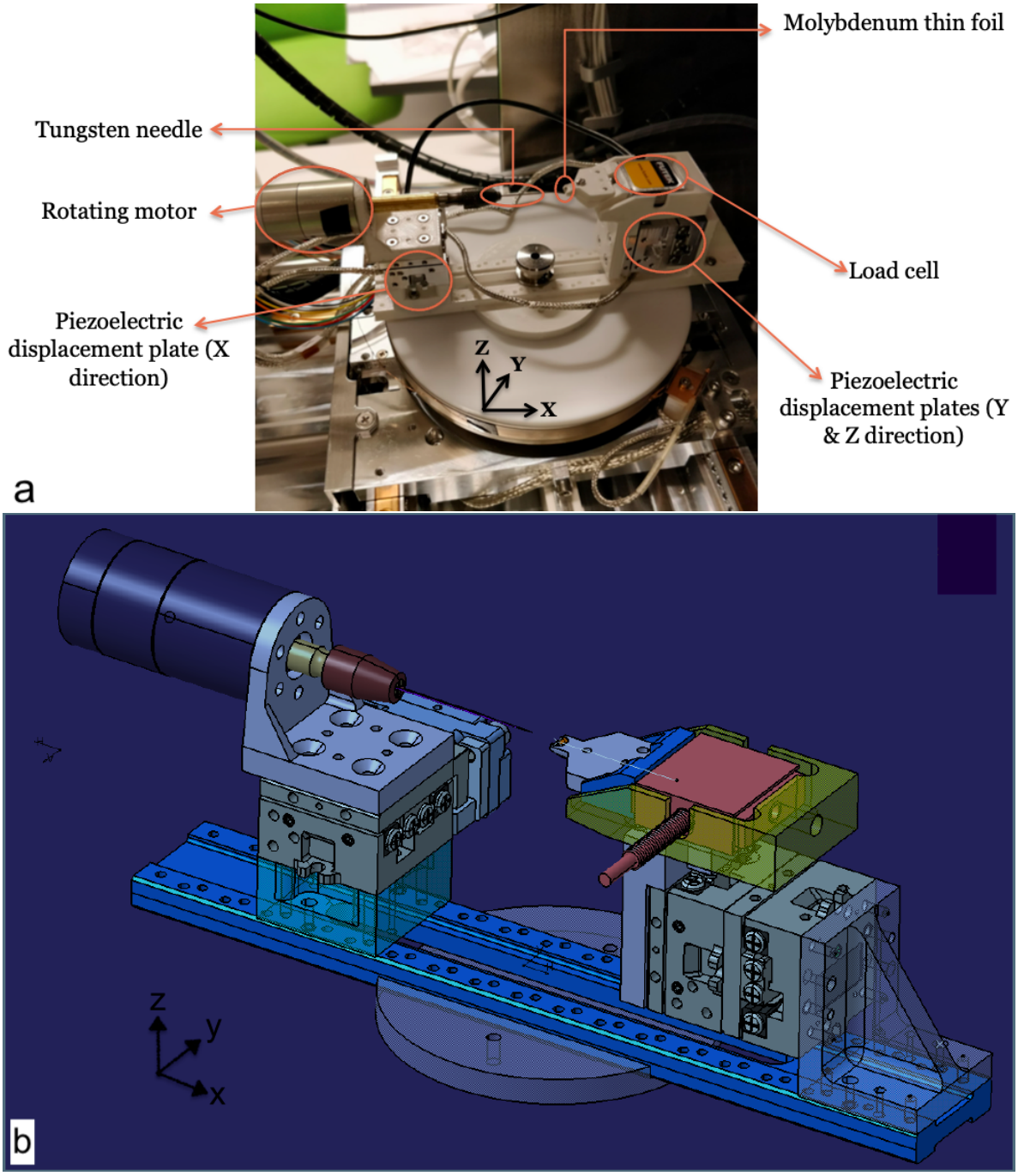

Figure 8: (a) In-situ micro-tensile testing machine (b) 3D representation of the in-situ micro-tensile testing machine.

In addition to the specimen machining, it was also possible with the help of the needle rotation to perform electronic and ionic images and Electron Backscatter Diffraction (EBSD) measurements on the specimen surfaces to confirm the position of the different layers within the specimen and give data for crystal plasticity.

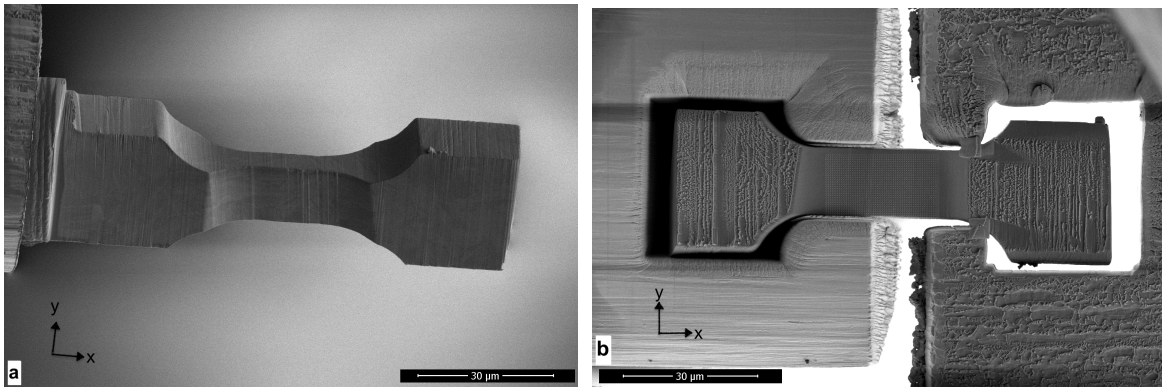

Figure 9: (a) 3D ionic machining of the specimen by rotating the needle (b) Tensile specimen after insertion in the grips and marking by platinum FIB deposition.

The second step consisted of the first grip machining in the Molybdenum thin foil. Then using the three piezoelectric displacement plates, the tensile specimen was inserted in the machined grip. In order to fix the specimen, the chamfers were welded to the grip with a platinum layer. In this configuration, the welds remained under compression during the tensile test to have a higher resistance. Once the specimen was fixed in the molybdenum grip, the second grip was machined in the rotating needle tip after ensuring that the tip diameter was suitable with the grip dimensions. The final step was the insertion of the second machined grip in the welded specimen head by using the three displacement plates (Fig. 9-b). It must be noted that the head was not welded to the second grip in order to ensure some flexibility for the specimen. A preload was also applied before each tensile test to align the specimen gauge length with the tensile direction and to minimize the off-axis loading during the test.

In order to measure the local and global plastic deformation during the tensile test, several arrays of platinum spots separated by 0.5 μm were induced by FIB deposition on the surface of the specimen (Fig. 9-b) and high definition SEM images (3072 x 2048 pixels) were acquired at small strain intervals during the tests. CMV, a DIC software [25], was then used to calculate the displacement field in the specimen surface for each SEM image. The local plastic strain field and the average strain in the specimen were derived from the displacement field with CMV according to the method developed in [26].

Two dogbone tensile test specimens were machined in a weld sample from the same SS DMW mock-up as the macroscopic tensile specimens from section 3.2. The first machined specimen was extracted from the martensitic band in the longitudinal direction L (Fig. 10) and the gauge section dimensions (width = 15 μm, length = 35 μm and thickness = 6 μm) were chosen in order to obtain a homogeneous martensitic composition and to have an estimated failure load under the upper limit of 0.5N of the load cell (Fig. 11-a). It must be noted

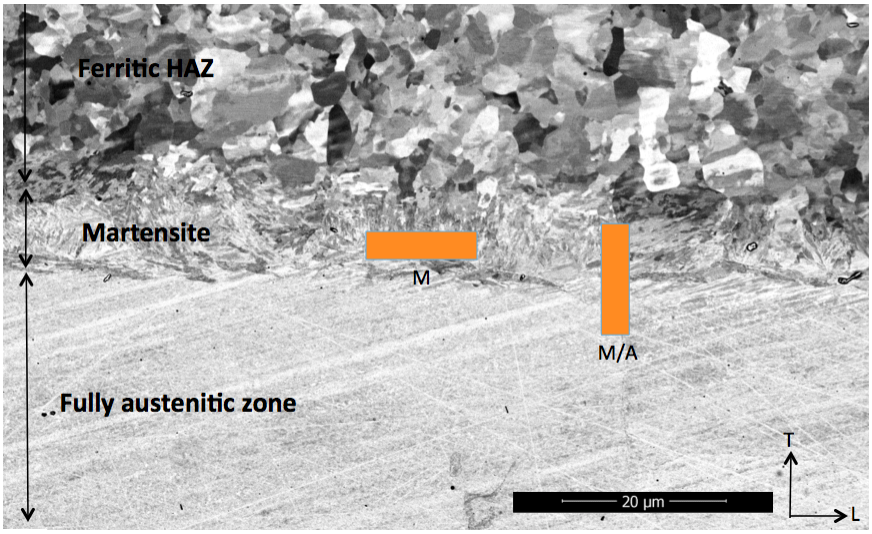

Figure 10: SEM image of 18MND5/309L interface after colloidal silica polishing (5 kV, BSE) and tensile specimens sampling (M : martensitic specimen, M/A : Martensite/Austenite specimen)

that an observation with secondary electrons given by ion scanning revealed the crystals boundaries of both the martensitic and austenitic parts of the specimens thanks to the channelling effect [27]. However, a long exposure to ion scanning had to be avoided in the austenitic steel since Ga^+ ions can induce a $\gamma \rightarrow \alpha$ transformation as it has been reported in [28, 29, 30].

The martensitic laths shown in figure 11-a confirm the homogeneity of the martensitic specimen. The second machined specimen (Fig. 11-b) was extracted in the martensite/austenite interface in the transverse direction T (Fig. 10) with the same dimensions to be able to use the same machined grips. Given the important size of the austenitic grains in the fully austenitic zone (up to 100 μm), it was not possible to have more than a single austenitic crystal from the carburized austenite in the specimen which we can clearly distinguish from the martensitic laths in the martensitic side (Fig. 11-b). The martensite/austenite interface also seems to be very irregular, being well centered on the upper side of the specimen and shifted to the austenitic side in the lower side.

The homogeneity of the martensitic specimen was confirmed by EDS after testing by comparing the measured local chemical composition in the specimen to EDS measurements in the martensitic band from a macroscopic weld sample shown in figure 3-b. In addition to EDS probing, EBSD was performed on the martensite/austenite specimen to confirm the interface localization and to obtain the austenitic crystal orientation. The austenitic grain had a ~[102] orientation along the normal direction (perpendicular to the specimen surface) and a ~[001] orientation along the tensile axis. The corresponding maximum Schmid factor along the tensile axis of the specimen was equal to 0.49, indicating that the austenitic crystal orientation was favorable to slip systems

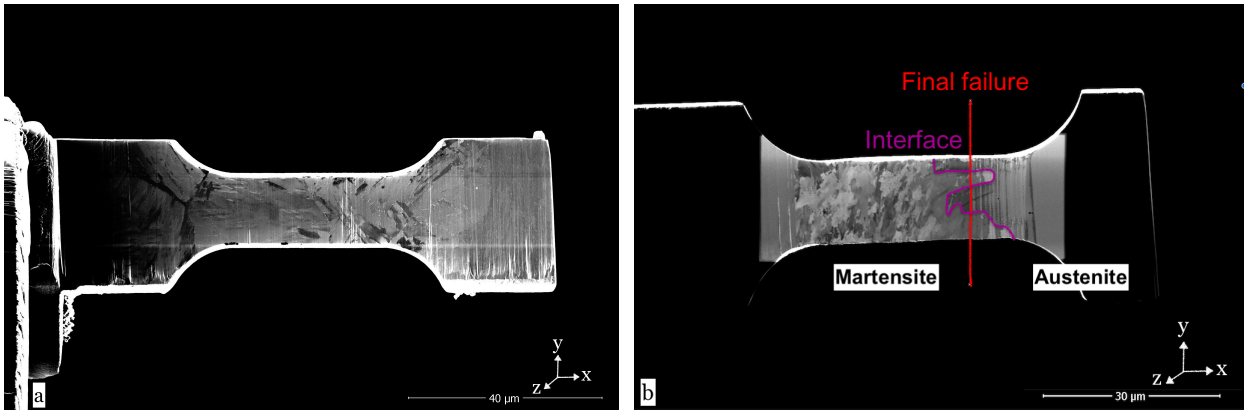

Figure 11: (a) Martensitic specimen before testing (b) Martensite/Austenite specimen before testing

activation and plastic deformation during the tensile test. It must be noted that the austenitic crystal orientation is in agreement with the solidification direction in the fully austenitic zone (along the temperature gradient so perpendicular to the ferritic-austenitic interface), which explains the important grain size.

4.3. Test results

The two specimens were tested to failure and videos of the tests were recorded. The displacement was held constant during the image acquisition and each pause was accompanied by a stress relaxation ranging from 5 to 10 MPa.

Figure 13-a shows the martensitic specimen after failure. Significant necking was exhibited in both specimens and shows that both materials have a ductile behavior reaching local plastic deformations (calculated for a square of 0.5 x 0.5 μm around each spot) around 30% for the martensitic specimen and 80% for the martensite/austenite specimen. For the bimaterial specimen, plastic deformation was concentrated in the austenitic side and the martensitic side remained elastic during the test (Fig. 12) and exhibited a higher resistance than the carburized austenite.

Moreover, the martensitic specimen reached failure immediately after the start of plastic deformation confirming the material's very small hardening capacity, while the austenitic side of the bimaterial specimen underwent significant work hardening after yield. The ductile behavior of the martensitic layer and carburized austenite was confirmed by the observation of the fracture surfaces of both specimens. Small dimples were observed in the martensitic specimen (Fig. 13-b) which are due to the numerous carbides in the material, while no clear dimples were observed in the carburized austenite which is due to the very large section necking.

For each test, a true strain-stress curve was calculated from the load cell data and the SEM images measure-

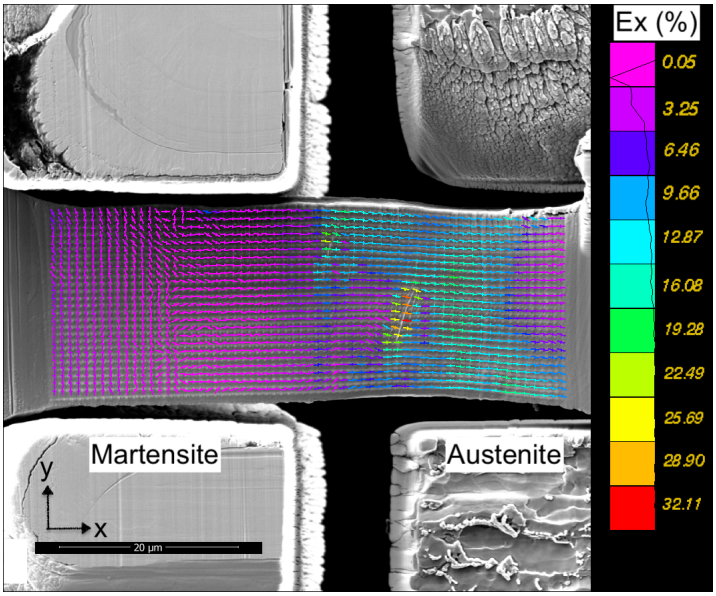

Figure 12: Strain repartition (along the x axis) in the Martensite/Austenite specimen in the necking phase (σ = 915 MPa (in the necking zone) et ϵ = 10,5%)

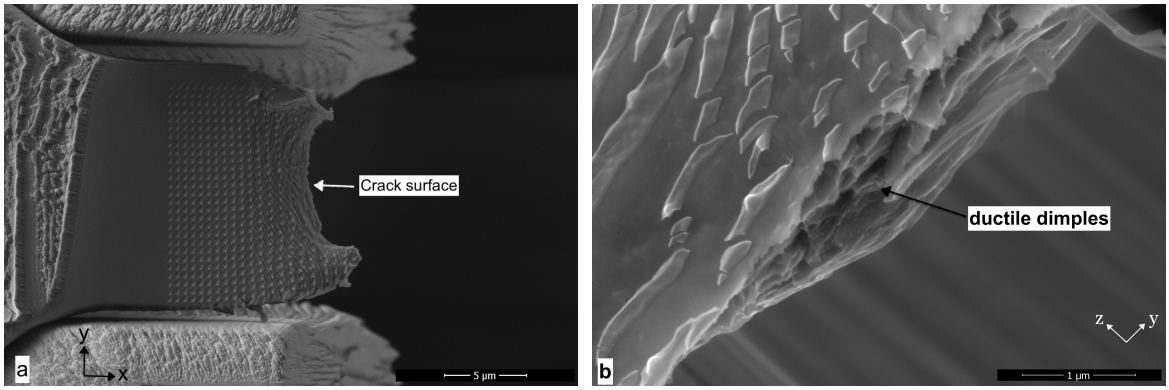

Figure 13: (a) Martensitic specimen after failure (b) crack surface of the martensitic specimen with ductile dimples

ments (Fig. 14-b). To calculate the true stress, the specimen section was measured for each image in the region where the final failure occurred by assuming that the relative variation of the specimen thickness is equal to the measured width variation (isotropic plastic behavior). For the true strain calculation, DIC measurements were possible only for a limited range of strain because of the rather high strain rate of both specimens compared to the SEM image acquisition time. For the martensitic specimen, no images could be taken in the plastic phase while for the martensite/austenite specimen, the last image taken before failure led to a calculated true strain of 10% (Fig. 14-a). Moreover, the thin FIB deposited Pt layer showed some cracks in the plastic phase for both specimens (Fig. 13), making post failure DIC measurements impossible in some parts of the specimen surface.

Three additional methods were therefore tested and compared to DIC measurements. The specimen gauge

section where final failure occurs, the gauge length and the distance between the two grips were measured for each SEM image taken during the test. Moreover, in order to characterize the specimens plastic behavior after the last SEM image taken, some additional images were taken from the test videos for greater strain values. The true strain was then calculated based on the variation of these three parameters using the following formula :

$$\epsilon_{section} = ln(\frac{S_0}{S}) \tag{4}$$

$$\epsilon_{length} = ln(\frac{l}{l_0}) \tag{5}$$

$$\epsilon_{grips} = ln(\frac{l_0 + \Delta d_g}{l_0}) \tag{6}$$

where $\epsilon_{section}$, ϵ_{length} and ϵ_{grips} are respectively the true strain calculated from the gauge section S, gauge length l and the variation of the distance between the grips Δd_g.

The different calculation methods were compared for the martensite/austenite specimen (Fig. 14-a). Only the austenitic side of the specimen was considered for the strain calculation, so the martensitic phase was not considered in the gauge length measurements or for strain calculation with the DIC software. Figure 14-a shows that DIC measurements are in a good agreement with strain calculation based on the section and gauge length variation, while the calculation based on the variation of the distance between the grips predicted higher strain values. This is due to the specimen slip in the grips in addition to the failure of the welds between the specimen and the molybdenum grip during the test. The strain calculation based on the specimen gauge section variation was finally selected to identify the constitutive laws for both the martensitic and carburized austenite layers.

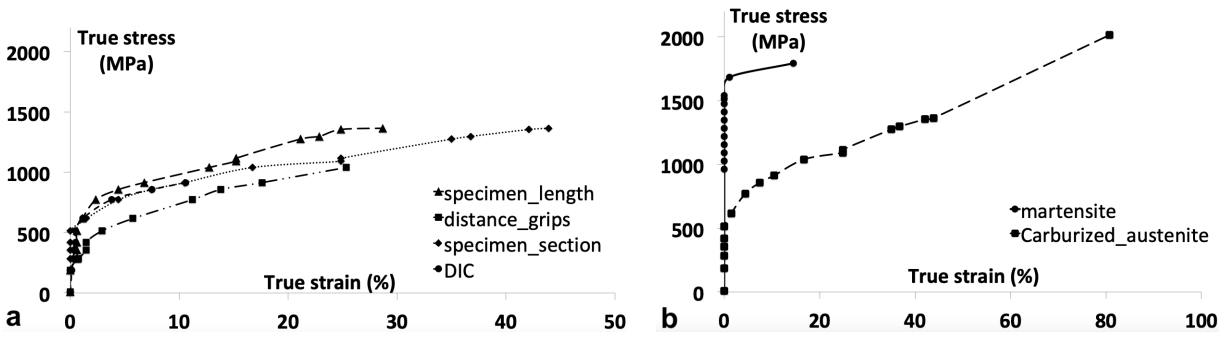

Figure 14: (a) Comparison between the different methods of true strain calculation for the carburized austenite (b) True strain-stress curves for martensite and carburized austenite

A Bridgman correction of the stress as in equation 3 was also applied for this test to take into account a possible multi axiality effect, but no significant difference was found.

Figure 14-b shows the true strain-stress curves for both tests. The martensitic specimen exhibited a yielding point at 1680 MPa (± 100 MPa) as there was a clear deviation from linear elasticity at a strain of ~1%. The maximum stress of 1900 MPa is reached at failure immediately after yield, so no hardening was measured for the martensite.

The second test characterized the carburized austenite since only the austenitic side of the specimen underwent plastic deformation, the martensitic side remaining elastic. The calculated true stress at specimen failure in the martensitic side of the specimen was only ~900 MPa which is smaller than the yield strength of 1680 MPa calculated for martensite in the first test. It must be pointed that for this test, final failure occurs in a plane mixing carburized austenite and martensite (Fig. 11-b), which was tracked by the FIB deposition marking. For the carburized austenite, a clear deviation from linear elasticity is measured at a strain of ~1.5% and a stress of 620 MPa. The yielding point was confirmed by DIC measurement as a clear disparity between strain values in martensite and carburized austenite initiated at that point. The austenitic side then underwent an important work hardening (n = 0.25) and reached a stress of ~2000 MPa at failure. The final reached stress was therefore greater than the yield strength of the martensitic layer which is in agreement with the specimen failure in both martensite and carburized austenite.

4.4. Discussion

The values obtained with these two tests conducted at a micron scale are globally in a good agreement with the other characterization methods. However, these values offer only a qualitative indication of the plastic behavior of the martensitic layer and the carburized austenite. The size-dependance of crystal plasticity has not been investigated in this study and the effect of the grains number and orientation should be consequent at this scale. For the martensitic layer, the grain size (<10 μm) is small compared to the specimen size, so the test should be representative of the macroscopic behavior. For the carburized austenite however, the specimen contained a single austenitic crystal, making the plastic behavior dependent on the crystal orientation and size. With that being said, the same tensile test could be numerically simulated with other austenitic crystal orientations using crystal plasticity data on the same material grade. Furthermore, the mechanical behaviors of single crystal specimens and polycrystals were compared by Vo [22] for a 304 stainless steel and a very good agreement was found.

Il must be noted that the yield stress calculated from the bimaterial tensile test and associated to carburized

austenite (620 MPa) is smaller than the value obtained by nanoindentation (1000 MPa in the second subregion), which is mainly due to the advantageous austenitic crystal orientation along the tensile axis. The anisotropic behavior of the carburized austenitic layer is also another factor which contributes to the deviation of nanoindentation stress-strain state from uniaxial tensile test. Weaver et al. [**?**] showed in fact that the scaling factor which represents the difference of stress state between indentation and uniaxial deformation depends on the material anisotropy. Therefore, for an unirradiated 304 stainless steel, a modification of the stress-scaling factor from 2.2 to 2.9 was necessary to obtain a good agreement between spherical nanoindentation and uniaxial tensile test stress-strain curves.

In this case, the introduction of a stress-scaling factor is not sufficient to obtain a good agreement between nanoindentation and micro-tensile testing curves since the measured work hardening exponent of the carburized austenite is also quite different between both methods (0.25 for the micro-tensile test and 0.12 for nanoindentation). The important work hardening during the micro-tensile test is likely due to a slight overestimation of stress values during the necking phase. Indeed, considering the fact that the plane where necking and failure occurs is composed of both martensite and carburized austenite, stress distribution is likely to be heterogenous in the final failure plane during the necking phase with smaller values in the less resistant zone, which is the austenitic crystal.

For the martensitic layer, the test results are in a very good agreement with nanoindenation (1680 MPa vs 1650 MPa) and also with macroscopic tensile testing. Both methods also predicted the small work hardening capacity of this layer.

We can therefore conclude that In-situ tensile testing is a very promising technique for plastic behavior characterization of small scale materials. This technique has also the benefit of characterizing the materials up to failure which allows the analysis of the failure mechanisms.

5. Conclusion

In this study, an in-situ tensile testing device was developed for meso-scale specimens and used to characterize a stainless steel dissimilar metal weld. Tensile specimens from the martensitic band and the carburized austenitic layer were tested to obtain a qualitative indication of the elasto-plastic behavior of the DMW hard layer. The yield stress and hardening exponent were extracted from the calculated true strain-stress curves. A yield stress of 1680 MPa was calculated for the martensitic band and no hardening was observed whereas the carburized austenite exhibited a softer behavior with a yield stress of 620 MPa and an important work hardening (n = 0.25). These values correlated well to literature values obtained by nanoindentation for the martensitic

band whereas a significant deviation was observed between both techniques for the carburized austenitic layer, which is due to orientation effects and to the material anisotropy.

The tensile testing machine also enabled specimens fabrication and manipulation, EBSD before testing and load and displacement measurements during testing. The crack surfaces were analyzed after testing and showed a ductile behavior for both martensite and carburized austenite. An approximative value for strain and stress to failure were also obtained for both materials, which is not accessible by other micromechanical techniques such as nanoindentation.

The mechanical behavior of the hard layer was also characterized with macro-scale tensile tests, using laser assisted local diameter measurements, on heterogeneous crossweld specimens machined perpendicularly to the ferritic-austenitic interface. The numerical modeling of these tests made it possible to obtain a yield stress value for the hard layer with an inverse identification method and it was found that the calculated values with micro-scale tensile tests are in good agreement with macro-scale tensile tests.

Acknowledgements

This work was carried out within the MATMECA consortium and supported by the ANR under contract number ANR-10-EQPX-37.

The presented study was sponsored by Framatome with the participation of the MSSMat and CEA/LISN laboratories. The authors wish to express their gratitude to all the partners who contributed in this work, especially Olivier Ancelet and Gregory Perez (CEA/LISN) for their help and contribution in the experimental program on the DMW mock-up, Éric Perrin and Frédéric Douit (MSSMat) for their great participation in the in-situ tensile testing machine development and all the Material research team of MSSMat for their helpful advices.

References

[1] Mas, F., 2014. Solidification and phase transformations in a dissimilar steel weld 18MND5/309L/308L : evolution of microstructure and mechanical properties. PhD. Grenoble University.

[2] Mas F., Martin G., Lhuissier P., Bréchet Y., Tassin C., Roch F., Todeschini P., Simare A., 2016. Heterogeneities in local plastic flow behavior in a dissimilar weld between low-alloy steel and stainless steel. Materials Science & Engineering A 667, 156-170.

[3] Mas F, Tassin C., Valle N., Robaut F., Charlot F., Yescas M., Roch F., Todeschini P., Brchet Y., 2016. Metallurgical Characterization of coupled carbon diffusion and precipitation in dissimilar metal welds. Journal of Materials Science 51 (10), pp.4864 - 4879.

[4] Gilles P., Robin V., Fontaine M., 2009. Welding residual stress effect on dissimilar metal weld junction fracture. Conference: ICPVT.

[5] Blouin, A., S. Chapuliot, S. Marie, C. Niclaeys, J.-M. Bergheau, 2014. Brittle fracture analysis of Dissimilar Metal Welds. Engineering Fracture Mechanics 131, 58–73.

[6] Faidy C., 2004. Structural integrity of dissimilar welds : ADIMEW project overview. Proceedings of PVP 2004, ASME Pressure Vessel and Piping Conference, 2004, USA.

[7] Gilles Ph., Devaux J., Faidy C., 2004. ADIMEW project: Prediction of the ductile tearing of a cracked 16 dissimilar welded junction. Proc. of PVP2004, ASME Pressure Vessel and Piping Conference, 2004, USA.

[8] Klueh, R.L., King, J.F., 1982. Austenitic stainless steel - ferritic steel weld joint failures. Welding Journal 61, 302–311.

[9] Sun, Z., Moisio, T., 1994. Weld metal/ferritic steel interface in laser welded austenitic/ferritic dissimilar steel joints. Journal of Materials Science Letters 13, 802–805.

[10] Gittos, M.F., Gooch, T.G., 1992. The interface below stainless steel and nickel-alloy claddings. Welding Research Supplement, 461s–472s.

[11] Gauzzi, F., Missori, S., 1988. Microstructural transformations in austenitic-ferritic transition joints. Journal of Materials Science 23, 782–789.

[12] Duppont J. N., Kusko C. S., 2007. Technical Note: Martensite Formation in Austenitic/Ferritic Dissimilar Alloy Welds. Welding Journal, 51s-54s.

[13] Murugan, N., Parmar, R.S, 1997. Effect of welding conditions on microstructure and properties of type 316L stainless steel submerged arc cladding. Welding Research Supplement, 210s–217s.

[14] J.L. Bucaille, S. Stauss, E. Felder, and J. Michler, 2003. Determination of plastic properties of metals by instrumented indentation using different sharp indenters. Acta Materialia 51, 1663-1676.

[15] Hosemann P., Kiener D., Wang Y., Maloy S.A., 2012. Issues to consider using nanoindentation on shallow ion beam irradiated materials. Journal of Nuclear Materials 425, 136-9.

[16] Kasada R., Takayama Y., Yabuuchi K., Kimura A., 2011. A new approach to evaluate irradiation hardening of ion-irradiated ferritic alloys by nano-indentation techniques. Fusion Engineering and Design 86, 2658-61.

[17] Ancelet, O., Matheron, P., 2010. Development of a new measurement system for tensile testing. PVP2010-25667, Bellevue; 2010.

[18] www.cast3m.cea.fr.

[19] Kiener D, Grosinger W, Dehm G, Pippan R, 2008. A further step towards an understanding of size-dependent crystal plasticity: In-situ tension experiments of miniaturized single-crystal copper samples. Acta Materialia 56, 580-92.

[20] Bhattacharyya D, Wheeler RW, Harrison RP, Edwards L, 2014. The Observation of Slip Phenomena in Single Crystal Fe Samples During In Situ Micro-Mechanical Testing Through Orientation Imaging. Microscopy and Microanalysis 20, 1060-9.

[21] Reichardt A., Ionescu M., Davis J., Edwards L., Harrison R. P., Hosemann P., Bhattacharyya D., 2015. In situ micro tensile testing of He+2 ion irradiated and implanted single crystal nickel film. Acta Materialia 100, 147-154.

[22] Vo H.T., Reichardt A., Frazer D., Bailey N., Chou P., Hosemann P., 2017. In situ micro-tensile testing on proton beam-irradiated stainless steel. Journal of Nuclear Materials 493, 336-342.

[23] Katsuhiko F., Fukuya K., 2011. Development of Micro Tensile Method in an FIB System for Evaluating Grain Boundary Strength. Materials Transactions 52, 20-24.

[24] Ben Salem, G., 2019. Brittle fracture of stainless steel dissimilar metal welds in the brittle-to-ductile transition range. PhD. Paris Saclay University.

[25] Bourcier M., Bornert M., Dimanov A., Héripré E., Raphanel J. L, 2013. Multiscale experimental investigation of crystal plasticity and grain boundary sliding in synthetic halite using digital image correlation. Journal of Geophysical Research: Solid Earth Volume 118, Issue 2, 511-526.

[26] Allais L., Bornert M., Bretheau T., Caldemaison D., 1994. Experimental characterization of the local strain field in a heterogenous elastoplastic material. Acta metall. mater. 42, No. 11, 3865-3880.

[27] Giannuzzi L.A., Michael J.R., 2012. Ion channelling vs. electron channelling image contrast. Microsc Microanal 18 , 694-695.

[28] Prasath Babu R., Irukuvarghula S., Harte A., Preuss M., 2016. Nature of gallium focused ion beam induced phase transformation in 316L austenitic stainless steel. Acta Materialia 120, 391-402.

[29] Basa A., Thaulow C., Barnoush A., 2013. Chemically induced phase transformation in austenite by focused ion beam. Metallurgical Mater. Trans. A 45 (3) 1189-1198.

[30] Knipling K.E., Rowenhorst D.J., Fonda R.W., Spanos G., 2010. Effects of focused ion beam milling on austenite stability in ferrous alloys. Mater. Charact. 61 (1) 1-6.

[31] Weaver J.S., Pathak S., Reichardt A., Vo H.T., Maloy S.A., Hosemann P., Mara N.A., 2017. Spherical nanoindentation of proton irradiated 304 stainless steel: A comparison of small scale mechanical test techniques for measuring irradiation hardening. Journal of Nuclear Materials. 493, 368-379.